Science of the Total Environment 466–467 (2014) 864–870

Contents lists available at ScienceDirect

Science of the Total Environment

journal homepage: www.elsevier.com/locate/scitotenv

Colloidal stability of nanoparticles derived from simulated cloud-processed mineral dusts

Enikö Kadar [a,*], Andrew Fisher [b], Björn Stolpe [c], Sergio Calabrese [d], Jamie Lead [c,e], Eugenia Valsami-Jones [c], Zongbo Shi [c]

[a] Plymouth Marine Laboratory, Prospect Place, The Hoe, Plymouth PL1 3DH, UK
[b] School of Geography, Earth and Environmental Sciences, University of Plymouth, Drake Circus, Plymouth PL4 8AA, UK
[c] School of Geography, Earth and Environmental Sciences, University of Birmingham B15 2TT, UK
[d] Dipartimento di Scienze della Terra e del Mare (DiSTeM), University of Palermo, Via Archirafi 36 Palermo, 90123, Italy
[e] SmartState Center for Environmental Nanoscience and Risk (CENR), Department of Environmental Health Sciences, Arnold School of Public Health, University of South Carolina, SC 29028, USA

HIGHLIGHTS

- Laboratory simulation of cloud processing of mineral dusts (CPMD) was conducted.
- The resulting nanoparticles (NPs) were characterized for colloidal stability.
- Acid-leachable Fe in volcanic ash is orders of magnitude higher than desert dust.
- Average size of newly formed nanoparticles increases when CPMD is in dark.
- Relative Fe % in the particles derived from CPMD is higher than in unprocessed dust.

GRAPHICAL ABSTRACT

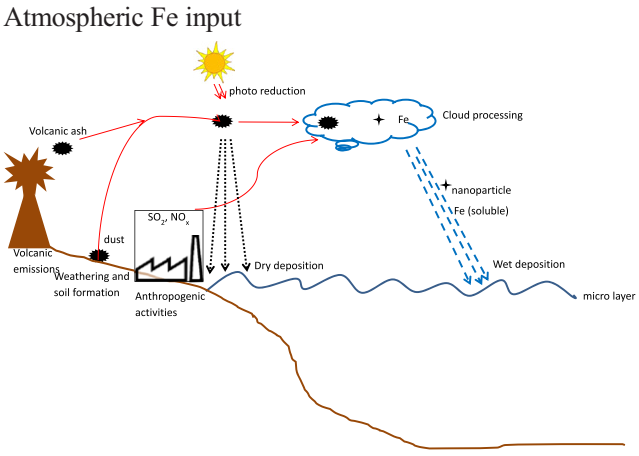

ARTICLE INFO

Article history:
Received 16 July 2013
Received in revised form 29 July 2013
Accepted 29 July 2013
Available online 25 August 2013

Editor: D. Barcelo

Keywords:
Atmospheric deposition
Ferrihydrite
Nanoparticle
Dissolution

ABSTRACT

Laboratory simulation of cloud processing of three model dust types with distinct Fe-content (Moroccan dust, Libyan dust and Etna ash) and reference goethite and ferrihydrite were conducted in order to gain a better understanding of natural nanomaterial inputs and their environmental fate and bioavailability. The resulting nanoparticles (NPs) were characterised for Fe dissolution kinetics, aggregation/size distribution, micromorphology and colloidal stability of particle suspensions using a multi-method approach. We demonstrated that the: (i) acid-leachable Fe concentration was highest in volcanic ash (1 mMg^{-1} dust) and was followed by Libyan and Moroccan dust with an order of magnitude lower levels; (ii) acid leached Fe concentration in the <20 nm fraction was similar in samples processed in the dark with those under artificial sunlight, but average hydrodynamic diameter of NPs after cloud-processing (pH ~ 6) was larger in the former; iii) NPs formed at pH ~ 6 were smaller and less poly-disperse than those at low pH, whilst unaltered zeta potentials indicated colloidal instability; iv) relative Fe percentage in the finer particles derived from cloud processing does not reflect Fe content of unprocessed dusts (e.g. volcanic ash > Libyan dust).

* Corresponding author. Tel.: +44 1752 633450; fax: +44 1752 633101.
E-mail address: enik@pml.ac.uk (E. Kadar).
URL: http://www.pml.ac.uk (E. Kadar).

0048-9697/$ – see front matter
http://dx.doi.org/10.1016/j.scitotenv.2013.07.119

The common occurrence of Fe-rich "natural nanoparticles" in atmospheric dust derived materials may indicate their more ubiquitous presence in the marine environment than previously thought.

1. Introduction

Atmospheric dust is a critical component of the Earth system as it affects climate not only by altering the atmospheric radiation budget but also by influencing the biogeochemical cycles in the ocean and in land via deposited dust (Okin et al., 2011). Atmospheric iron deposition for instance, is a well-established mechanism for increasing the productivity in iron-limited areas of the ocean, and the artificial ocean iron fertilisation and subsequent controlling variable for CO_2 pump (Buesseler, 2012; Smetacek et al., 2012). The "iron hypothesis" has been tested and supported through in situ iron fertilization experiments in the iron limited, i.e. high nutrient low chlorophyll regions of (Smetacek et al., 2012; Wolff et al., 2011; Boyd et al., 2000; Coale et al., 1996), which resulted in clear and unambiguous physiological responses to the addition of iron— massive phytoplankton bloom of predominantly diatoms. Moreover, addition of iron in the nano-particulate form is likely to produce results of higher impact than the bulk Fe salts owing to the metal's improved reactivity/bioavailability when in nano-form (Raiswell et al., 2008; Kadar et al., 2013). However, before any such application involving nano iron discharge to the marine environment is endorsed the possible impacts need to be thoroughly investigated. Moreover, natural nanomaterial inputs and studying their bioavailability and effects are important not only from a biogeochemical standpoint, but also could provide important data for nanotechnology.

It has been shown that the chemical processes likely to take place in clouds generate nanoparticulate iron from mineral dusts (Shi et al., 2009, 2011a, b). Such dust-derived "natural nanoparticles" could thus represent an important portion of bioavailable iron, and although investigation of their mineralogy and physico-chemistry has started we do not understand how marine organisms might take up nano forms of the metal. Also, atmospheric nanoparticles (NPs) and soluble Fe undergo substantial transformations immediately in contact with seawater (such as aggregation, photo reduction, dissolution and interaction with natural organic matter) before becoming available for biological uptake by marine phytoplankton. These reactions often take place too rapidly to be quantified in the field and thus pertinent field data is lacking to date. The main objective of this work is to provide insight to the environmental fate and behaviour of metal-rich natural NPs from cloud-processed mineral dusts. Thus we have performed simulated cloud processing of three model dusts and we characterise the physicochemical transformations that take place while dust particles are cloud processed and when in contact with seawater under environmentally relevant conditions in the laboratory with carefully controlled experimental conditions.

The kinetics of iron dissolution from mineral dusts under conditions closely simulating atmospheric aerosol processes have previously been analytically quantified (Shi et al., 2009, 2011a, b) or predicted by dissolution models (Fan et al., 2006; Meskhidze et al., 2005; Luo et al., 2005), but results are inconsistent owing mostly to the complex Fe mineralogy in natural dusts and other physical characteristics. These, combined with the influence of weathering/ageing processes at the site of dust source, control the potential of Fe to be solubilised, making predictions of a general dissolution behaviour particularly challenging (Shi et al., 2011b). Common conclusions from these studies indicate the existence of more than one Fe pool within mineral dusts with distinct dissolution kinetics and highlight the importance of pH, dust/liquid ratio and grain size as the main factors influencing Fe dissolution kinetics (Shi et al., 2011b; Boyd et al., 2010).

Whilst the processes involved in the atmospheric deposition of volcanic ash plumes are fundamentally similar to those of mineral dusts, only a few studies have focussed on the effect of volcanic ash on marine primary productivity (Hoffmann et al., 2012; Olgun et al., 2011; Langmann et al., 2010) and linked to climate forcing (Achterberg et al., 2013; Duggen et al., 2010). Direct trace metal input through seafloor volcanic activity has been recognised as an important source of oceanic dissolved iron (Sander and Koschinsky, 2011), regardless of the geo-tectonic setting: subduction zones (Tagliabue et al., 2010), ocean floor spreading centres (Kadar et al., 2005) or cold seeps (Kadar et al., 2012). Similarly, continental subduction and terrestrial hotspots can also discharge considerable amount of metals to the surface ocean via ash deposition (Hoffmann et al., 2012). Indeed, there is evidence for comparable iron discharge from volcanic ash with that from atmospheric dusts, i.e. 35–340 nM Fe g^{-1} ash and 20–200 nM Fe g^{-1} dust, for dry deposition during the first hour of contact with seawater (Olgun et al., 2011); although much higher concentrations were also reported (order of mM Fe g^{-1} ash) from leaching experiments on 48-h fresh lava from the Etna (Cimino and Toscano, 1998). Wet deposition field data showed significant effect of the natural ash Fe leaching on bulk deposition associated with the volcanic eruptions of the Etna, and which could be detected in environmental samples (Calabrese et al., 2011). However, exact Fe release from volcanic ash via cloud processing remains to be investigated.

This paper focuses on three model dust types with distinct Fe-content and is aimed at standardising a laboratory protocol for simulation of cloud processing (SCP) of mineral dusts and carefully characterising the resulting nanoparticulate material. Specifically, Fe dissolution/Fe lability, particle aggregation/size distribution, surface topology and zeta potential were characterised. In addition, we provide key information on methods suitable for characterisation of naturally present NPs.

2. Experimental

2.1. Dust samples

Soil samples from (a) Sahara, Morocco (30°16′N–4°55′W); (b) Libya (25°35′N–16°31′E) and (c) volcanic ash (un-weathered lapilli collected after eruption of Etna in July 2011; 37°44′N–14°59′E) collected and stored in plastic bags, were gently crushed on a mortar and dry-sieved (on plastic sieves of 90 μm mesh size); and (d) ferrihydrite and/or nano-goethite synthesised according to methods described earlier (Cornell and Schwertmann, 2003) were used as model iron oxides with known mineralogy (Shi et al., 2011a). Chemical compositions of the dust and ash samples were analysed by x-ray fluorescence spectrometry (XRF) and inductively coupled plasma optical emission spectrometry (ICP-OES) (Table 1). The XRF instrument used was the Rigaku ZSX primus, equipped with a tube in Rhodium and the crystal analysers (lif 200, 220, Rx25). After calculating the loss from ignition (LOI) on 1 g of sample, analysis was made on 2 g of sample, previously crushed, and added to the aluminium supports on a base of boric acid. The samples were compared with standard (certificates). Acid digests were obtained via microwave digestion (Mars Xpress) of about 250 mg powder sample in 2 mL of concentrated hydrochloric acid and 1 mL of hydrofluoric acid (all acid were ultrapure) using Teflon vials.

2.2. Fe dissolution and simulated cloud processing of dusts

The cloud simulation protocol was a modified version of the previously reported method (Shi et al., 2009) and consisted of a single acid

Table 1
Bulk chemical composition of dust and ash samples.

	Etna	Libya	Morocco
(%)			
SiO_2	48.55	43.89	95
Fe_2O_3	11.54	3.75	0.59
Al_2O_3	14.88	10.47	1.96
CaO	10.58	18.88	0.22
MgO	6.67	2.66	0.08
Na_2O	2.55	0.23	0.001
K_2O	1.74	1.9	0.35
TiO_2	1.54	0.5	0.04
P_2O_5	0.35	0.16	0.04
MnO	0.17	0.06	0.01
(ppm)			
Si	226729	204966	443650
Fe	80665	26213	4124
Al	78715	55386	10368
Ca	75647	134992	1573
Mg	40220	16040	482
Na	18906	1692	7
K	14 442	15770	2905
Ti	9225	2995	240
P	1526	698	174
Mn	1316	464	77
Sr	881.26	218.8	55.16
Ba	621.8	335.23	190.41
V	253.3	55.48	3.89
Zr	168.61	213.82	37.18
Cr	161	59	93
Ni	99.06	8.39	62.84
Zn	96.38	61.87	19.96
Ce	88.16	85.65	30.11
Cu	81.4	20.38	16.39
Rb	50.31	50.83	25.76
La	43.5	32.9	34.24
Co	38.27	8.81	–
Nb	34.7	11.65	–
Y	23.56	14.16	0.17
Pb	13.73	20.13	15.65

cycle of acidic (pH 2) and circum-neutral pH (pH 6). Experiments were conducted in triplicate for each dust sample and under darkness (i.e. HDPE flasks were covered with aluminium foil) unless otherwise described. In order to determine the Fe dissolution kinetics in our model mineral dusts the simulated cloud processing was performed on a dust/liquid load of 60 mg/L. This was chosen, based on previous pilots to optimise for maximum yield of nanoparticulate material. Briefly, suspensions of each pre-sieved dust (<20 μm) were made by adding 30 mg powder to 500 mL of 0.05 M H_2SO_4 solution (pH 2) and these were permanently stirred at a constant rate of 50 rpm, using a multi-position magnetic stirrer (Barnsted, UK). Aliquots of 2 mL were taken immediately after addition of dusts (T_0) and then after 1, 3, 6, 24, 48 and 96 h, and were filtered through 0.2 μm polycarbonate (PC) membranes (Millipore) prior to soluble Fe analysis by the Ferrozine method (Viollier et al., 2000). Samples and standards were prepared in HDPE tubes. All equipment had been carefully acid washed prior to use. All reagents were from Sigma Aldrich and at least analytical grade. All solutions were prepared in MQ water.

The remaining 486 mL suspensions were neutralised by drop-wise addition of concentrated ammonia solution (Sigma) to pH 6 (obtained within one minute). These suspensions were then pre-filtered on 0.45 μm pore size PC membranes to remove coarse material and then filtered through pre-weighed 200 and 50 nm pore-size polycarbonate filters, which were air-dried, and stored in Petri slides until further analysis using transmission electron microscope (TEM) and scanning electron microscope.

The influence of illumination on Fe dissolution from dusts during simulation of cloud processing was assessed using a sunlight simulator (2200 Lux with AquaGlo 20 W lamp; λ 380–780 nm) equivalent to surface oceanic conditions. Samples (5 mL) were taken in acid washed 5 mL syringes and filtered through 0.02 μm Anopore syringe filters (Anotop). The 4.5 mL filtrates were acidified with 0.5 mL of 67% HNO_3 until analysis by Inductively Coupled Plasma Mass Spectrometry (ICP-MS, Agilent 7500Cx, 3 USA) to determine the Fe concentration. Total Fe was also determined in equivalent subsamples processed similarly, but with a 0.2 μm filtration step. Samples and standards were prepared in HDPE tubes. All equipment had been carefully acid washed prior to use. All reagents were from Sigma Aldrich and at least analytical grade. All solutions were prepared in MQ water (Millipore).

2.3. (Nano) Particle characterisation

The average hydrodynamic diameter, zeta potential and poly dispersity index of particles at both pHs 2 and 6, on unfiltered samples were determined by dynamic light scattering (DLS) and electrophoresis using detection by laser Doppler velocimetry on a Malvern Zetasizer (Nano series, Malvern Instruments, UK).

Particle size distribution, shape and micro-morphology were studied by electron microscopy. TEM samples were prepared using previously reported method (Kadar et al., 2012). Briefly, re-suspension of the NPs retained by the 50 nm PC membranes, by sonicating each membrane in 2 mL methanol followed by drop deposition onto Formvar/carbon coated 50 mesh Cu grids (S162-3, AGAR Scientific). Particles were allowed to adsorb to the carbon coating for 10 min (without drying), followed by gently immersing the grids in ultra pure water to remove

un-adsorbed particles, and air-drying under protective cover. Electron micrographs were acquired using TEM at 80 keV (JEOL 1200EX). At least ten micrographs were taken from various locations of the grids (to ensure representativeness), and particle size and shape parameters were evaluated using image analysis computer software (Digital Micrograph, Gatan Inc.). High-resolution micrographs of selected particle-types were also acquired on a TEM operating at 200 keV (Philips Tecnai F20).

Scanning electron microscopy samples were prepared by carbon coating (for 2 min on Emitech K450X) of small pieces of each membrane (both 50 and 200 nm pore sizes) and observed on a JEOL-JSM 7001 F (Oxford Instruments) scanning electron microscope with X-ray detector. Electron micrographs were taken of at least 25 typical particles along a random transects and particles were scanned for elemental composition.

3. Results and discussion

3.1. Chemical compositions of dust and ash samples

Elemental composition of the three unaltered dust samples measured by XRF (Table 1) indicates distinct geochemical composition with an order of magnitude difference in their iron oxide percentage. Total Fe concentrations were markedly different with the highest content in Etna ash (>80000 ppm) followed by the Libyan dust (>26000 ppm) and Moroccan dust (>4000 ppm), consistent with previous reports (Shi et al., 2011a).

3.2. Fe dissolution kinetics from geochemically distinct mineral dusts and volcanic ash

The dissolution of Fe from dusts at pH 2, operationally defined here as the concentration of Fe in the 0.2 μm filtrates, was fastest during the first 3 h of SCP (Fig. 1 inset) with the highest concentration of dissolved Fe being released from the volcanic ash from Etna (260 ± 7 μMg^{-1}) followed by goethite (18 ± 3 μMg^{-1} Fe), Libyan dust (19 ± 8 μMg^{-1}) and Moroccan dust (11 ± 6 μMg^{-1} Fe), respectively. The dissolution has slowed down after 48 h but only reached a plateau for the volcanic ash samples (Etna). This is consistent with the duration of the "fast and intermediate Fe pools" previously reported (Shi et al., 2011a), but may also be due to the distinct Fe concentrations in the dusts. Both the Libyan and Moroccan dusts showed similar dissolution profiles to the reference goethite model. The fast and intermediate Fe pools may be primarily composed of poorly crystalline Fe(III) oxyhydroxides and/or little reactive dry ferrihydrite and nano-sized Fe oxides (Shi et al., 2011a). However, Fe dissolution rates from the volcanic ash are an order of magnitude higher possibly owing to the presence of original Fe(II) minerals in volcanic ash (Olgun et al., 2011; Cimino and Toscano, 1998), which are more soluble than Fe(III)oxides (Delmelle et al., 2005).

The comparison of iron dissolution, i.e. the concentrations of soluble and nanoparticulate phases (<20 nm) generated from the three types of dusts at pH 2 after 96 h, via SCP under darkness vs. simulated sunlight (Fig. 2) showed total concentrations and the ratio between particles smaller and larger than 20 nm markedly different for the three dust types. These relative differences remained unaltered in the presence of artificial sunlight (Fig. 2A) with the only exception of Saharan dust (possibly due to a filtration artefact). Dissolution was highest in volcanic ash (49 mg Fe g^{-1} ash), while Moroccan and Libyan dust Fe contents were lower (0.4 and 0.8 mg Fe g^{-1} dusts, respectively). In the absence of light, most important processes contributing to iron in the <20 nm filtrates are expected to be dissolution of Fe-rich minerals from the dust particles, and transfer of inherent <20 nm iron-rich nanoparticles from the dust to the liquid phase. In an irradiated system the solubility of Fe(III) minerals is expected to increase as a result of photo reduction to higher-solubility Fe(II), i.e., the reaction when a surface complexed hydroxyl group donates an electron to a photo excited surface Fe(III) atom (Miller et al., 1995). Curiously this was not the case here and in other studies (Rose and Waite, 2003). Similarly, the lack of an amplified solubility in

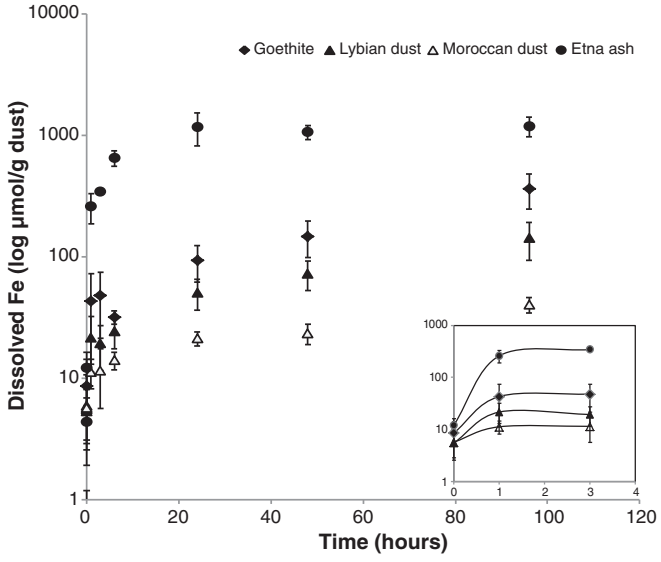

Fig. 1. Iron (Fe) dissolution kinetics of Libyan dust, Moroccan dust, volcanic ash and nano-goethite at pH 2 and at dust/liquid ratio of 60 mgL^{-1} monitored over 96 h. Values are average ± standard error from mean (SEM), $N = 3$. The inset shows in more detail the first 3 h.

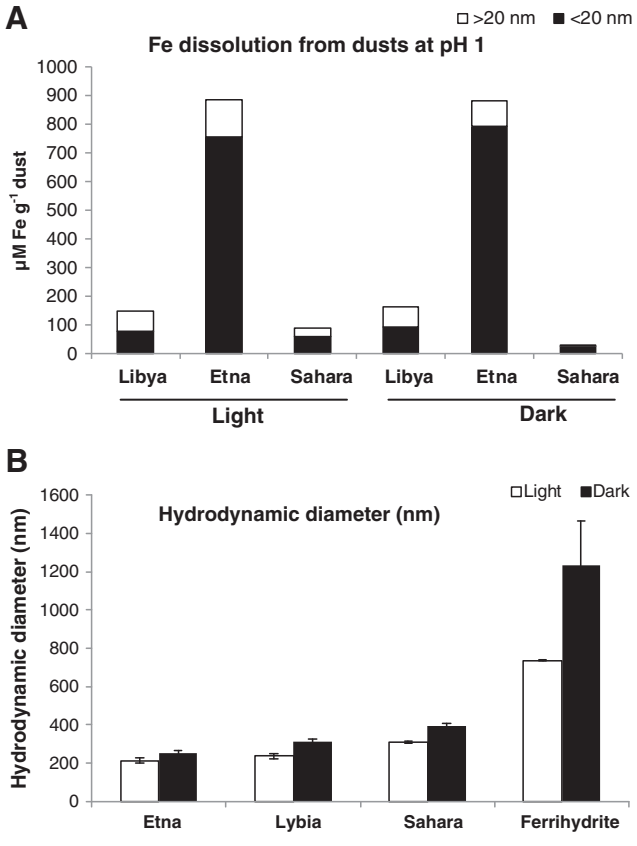

Fig. 2. Iron dissolution after acid processing (at pH 2) under darkness vs simulated sunlight of the three studied mineral dusts (volcanic ash from Etna, dust from Morocco and dust from Libya) expressed as A) dissolved Fe (>20 nm < 200 nm) with the <20 nm filter-passing fraction; B) average hydrodynamic diameter of particles resulting from simulated cloud processing at pH 6 (Bars represent average values ± SEM, $N = 5$).

irradiated systems compared to dark-processing was explained by competing timescales of the redox transformations (Rose and Waite, 2003). Another possibility could be that Fe in the <20 nm filter-passing fraction was largely associated with organic complexes or small nanoparticles. Dissociation of these <20 nm compartments as a result of photochemical reactions, followed by re-precipitation of iron oxyhydroxide to form >20 nm particles, could also disguise improved solubility in irradiated samples compared with those processed in the dark. Small dissimilarities may also be explained by few free radical formation in the solution due to low organic concentration of the seawater and also to the light source that did not include some of the UV wavelengths (i.e. below 380 nm).

The hydrodynamic diameters (zeta average diameter) of the particles formed during the simulated cloud processing (at pH 6) were determined using dynamic light scattering (DLS), which showed that average hydrodynamic diameters were in the range of 200 and 400 nm (Fig. 2B). The hydrodynamic diameters given by DLS are probably much larger than the number average diameter of the particles, since the DLS signal typically becomes dominated by large particles in polydisperse samples (Domingos et al., 2009). Even though DLS overestimates the average particle sizes, comparative data can give valuable information about their differences in particle size distribution and especially about the presence of larger particles in the samples. The DLS showed consistently larger hydrodynamic diameters when the simulated cloud processing was performed in the dark compared with under artificial sunlight in all dust types (Fig. 2B). The difference was the most noticeable for ferrihydrite, which also showed a considerably larger hydrodynamic diameter (700–1200 nm) than the natural dust samples (200–400 nm, Fig. 2B), which is most likely due to aggregation of the freshly forming individual ferrihydrite NPs known to have 6–10 nm diameter (Shi et al., 2009).

Although direct comparisons are difficult because of dissimilar experimental designs and different protocols used for dissolution experiments there are common trends seen in our data compared with those from previous studies (Shi et al., 2009, 2011a, b) including significant proportion of dusts are converted to NPs after simulated cloud processing (i.e. ~1% w/w data not shown here). Additionally, the Fe that leaches out from dusts into solution during simulated cloud processing forms nanoparticulate aggregates (as shown in Fig. 2A, over 50% of the acid leachable Fe from dusts were released in solution in the <20 nm fraction during the acidic phase, which then precipitated into nano-sized colloids).

3.3. Colloidal stability of cloud processed mineral dusts

When the pH in simulated cloud processed samples was increased from 2 to 6, the average hydrodynamic diameter (Fig. 3A) and polydispersity index (Fig. 3B) determined by DLS decreased dramatically for the natural dust samples and slightly for the ferrihydrite sample. The results are unexpected, since both iron oxyhydroxide and aluminium silicate particles are expected to acquire a lower charge density when the pH is raised from 2, which should result in increased aggregation and growth in size (Baalousha, 2009). However, no significant changes in zeta potential could be observed for the suspensions of natural dust, while a change from negative to positive zeta potential was observed for the ferrihydrite (Fig. 3C), implying that the surface charges of the natural dust particles were independent of pH. One possible explanation to our results is that some nanoparticles have aggregated when the pH was raised from 2 to 6, but that the particles formed were large enough to settle out of suspension, resulting in the observed decrease in hydrodynamic diameter and polydispersity index of the nanoparticle remaining in suspension. It is more likely that some of the components in natural dusts have instigated a different Fe dissolution/aggregation behaviour from those observed with the synthetic ferrihydrite.

3.4. Typical (nano) particles in geochemically distinct mineral dusts

The scanning electron micrographs of the dusts prior to SCP (Fig. 4A and E) revealed the presence of particles ranging in size from a few μm to several hundred μm and with large variation in micromorphology. However, following the SCP the particles that were retained on the 50 nm membranes (after pre filtration on the 0.2 μm membrane) were spherical and more similar in morphology (Fig. 4B and F). The EDX-spectra obtained on the 200 nm filtrates enabled calculation of the relative percentages of the main element constituents (Fig. 4C, and G). This technique can typically give semi-quantitative information about elemental composition when the element makes more than about 0.1–1.0% of the total mass of specific particles on the selected area (Utsunomiya and Ewing, 2003). The average elemental weight distribution (%) of Fe, O, Si, Al and S within the typical nano particles during the simulated cloud processing (Fig. 4C and G) showed higher Fe content in Libyan dust than in volcanic ash. It is also noticeable

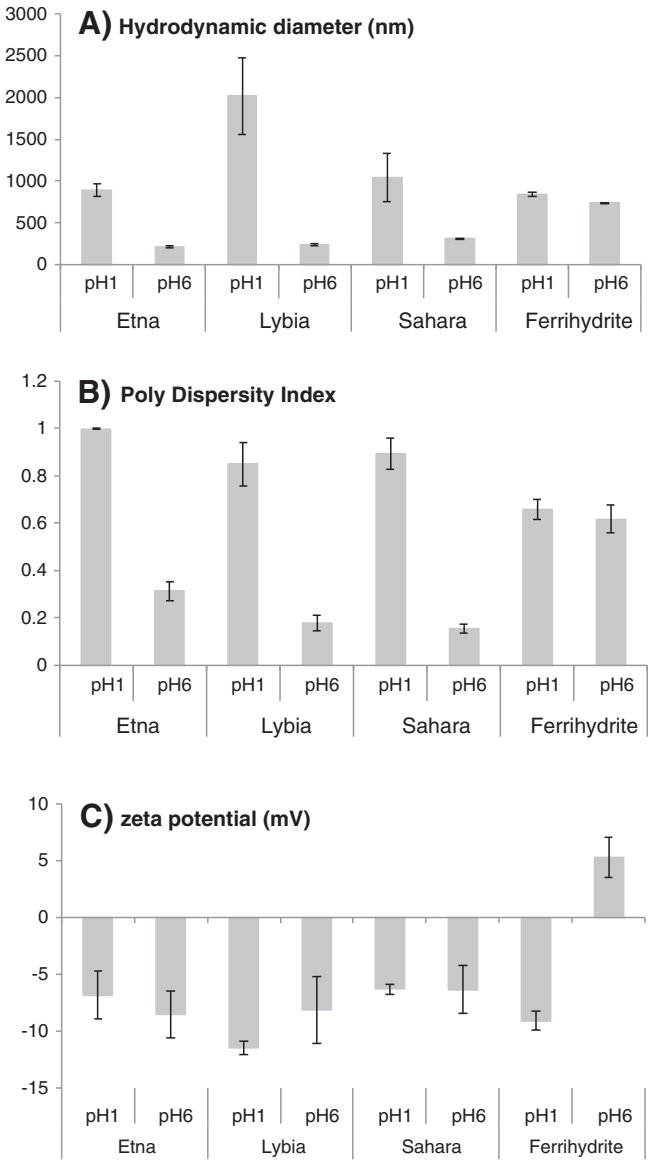

Fig. 3. Dynamic light scattering (DLS) analysis on nanoparticle suspensions during simulated cloud processing of volcanic ash from Etna, dusts from Morocco and Libya and ferrihydrite; A) average hydrodynamic diameter (nm) ± SEM, $N = 5$; B) polydispersity index ranging between 0 and 1, where 1 is equivalent to maximum particle heterogeneity; C) zeta potential based on 5 consecutive measurements of electrophoretic mobility in a cell containing 1 mL suspension.

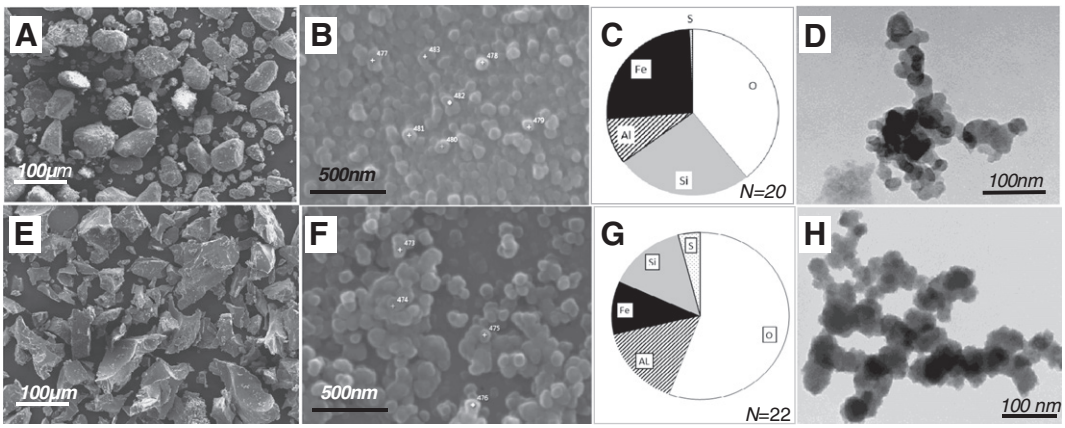

Fig. 4. Micromorphology and elemental composition of Lybian dust (A–D); and volcanic ash from Etna (E–H). Selected scanning electron micrographs of particles prior to (A and E) and following SCP (B and F) with their elemental composition estimated based on EDX spectra acquired from $N \geq 20$ typical particles at random locations of the membrane (C and G); TEM micrographs of typical nanoparticles retained on the 50-nm filter, re-suspended in absolute ethanol and allowed to settle on formwar coated Cu grids (D and H).

that the Fe percentage in the post-cloud processed particles derived from Lybian dust are higher than in the unprocessed dust sample (Table 1), whilst Fe% in volcanic ash remains unaltered by cloud processing. A higher Fe % in finer atmospheric materials compared to the parent dusts is consistent with environmental observations on desert dusts which are known to change in bulk chemical composition and particle size distributions while travelling through the atmosphere. Physical and chemical processes on the parental materials during transport will have an effect on particle size ranges and accessory minerals, which in turn control the chemical processes that favour augmented relative abundance of Fe and Al in the resulting finer materials (Castillo et al., 2008). Interestingly, TEM micrographs (Fig. 4D and H) show visible distinction in micromorphology of particles: Libyan dust produced spherical particles of 10–20 nm diameters that seemed to aggregate (possibly due to the effect of vacuum in the TEM chamber) (Fig. 4D); while the particles within the aggregates derived from volcanic ash had a more ragged aspect (Fig. 4H) showing coalesced spheroids with stumped pin cushion morphology similar to those described nanoparticulate schwertmannite from glacial sediments (Raiswell, 2011). The highly reactive sulphates and fluorides of iron and aluminium are commonly adsorbed on the surface of volcanic ash particles (Delmelle et al., 2007) and thus may be responsible for the more "ragged aspect" of the ash-derived NPs. This combined with the influence of different weathering/ageing processes at the source (i.e. volcanic lapilli vs. desert dust) can yield particles not only with distinct morphology but also reactivity, as illustrated by the Fe dissolution (Fig. 1).

To conclude, our study has confirmed the profuse presence of nanoparticles in suspension following simulated cloud processing of mineral dusts. Micromorphology of these particles closely resembles iron oxyhydroxide nanoparticulates from glacial and glaciomarine environments (Raiswell et al., 2008; Raiswell, 2011) whose acid-leachable Fe content is also comparable with those in atmospheric dust. The occurrence of Fe-rich "natural nanoparticles" in such distinct weathering environments and lithologies may indicate their more ubiquitous presence than previously thought. The larger scale implications at real ecosystems level are at the primary productivity level with serious ecological and economic implications. Given the important ecological role of primary producers in Fe-limited areas of the global ocean it is likely that atmospheric dust-input increases phytoplankton biomass to such extent that it can potentially affect the structure, productivity, function and diversity of these marine ecosystems.

Conflict of Interest

No conflict of interest.

Acknowledgment

The Natural Environment Research Council (NERC) funded facility FENAC at the University of Birmingham is acknowledged for their help with microscopy analysis (FENAC/2012/02 grant to EK).

References

Achterberg EP, Moore CM, Henson SA, Steigenberger S, Stohl A, Eckhardt S, et al. Natural iron fertilisation by the Eyjafjallajökull volcanic eruption. Geophys Res Lett 2013;40:921–6.
Baalousha M. Aggregation and disaggregation of iron oxide nanoparticles: influence of particle concentration, pH and natural organic matter. Sci Total Environ 2009;407:2093–101.
Boyd PW, Watson AJ, Law CS, Abraham ER, Trull T, Murdoch R, et al. A mesoscale phytoplankton bloom in the polar Southern Ocean stimulated by iron fertilization. Nature 2000;407:695–702.
Boyd PW, Mackie DS, Hunter KA. Aerosol iron deposition to the surface ocean – modes of iron supply and biological responses. Mar Chem 2010;120:128–43.
Buesseler KO. Biogeochemistry: the great iron dump. Nature 2012;487:305–6.
Calabrese S, Aiuppa A, Allard P, Bagnato E, Bellomo S, Brusca S, et al. Atmospheric sources and sinks of volcanogenic elements in a basaltic volcano. Etna, ItalyGeochim Cosmochim Acta 2011;75:7401–25.
Castillo S, Moreno T, Querol X, Alastuey A, Cuevas E, Herrmann L, et al. Trace element variation in size-fractionated African desert dusts. J Arid Environ 2008;72:1034–45.
Cimino G, Toscano G. Dissolution of trace metals from lava ash: influence on the composition of rain water in the Mount Etna volcanic area. Environ Pollut 1998;99:389–93.
Coale KH, Johnson KS, Fitzwater SE, Gordon RM, Tanner S, Chaves FP, et al. A massive phytoplankton bloom induced by ecosystem-scale iron fertilization experiment in the equatorial Pacific Ocean. Nature 1996;383:495–501.
Cornell RM, Schwertmann U. The iron oxides: structure, properties, reactions, occurrences and uses. Weinheim: Wiley-VCH Verlag Gmbh&co; 2003.
Delmelle P, Lambert M, Dufrêne Y, Gerin P, Óskarsson N. Gas/aerosol–ash interaction in volcanic plumes: new insights from surface analyses of fine ash particles. Earth Planet Sci Lett 2007;259:159–70.
Domingos RF, Baalsousha MA, Ju-Nam Y, Reid MM, Tufenjki N, Lead JR, et al. Characterizing manufactured nanoparticles in the environment: multimethod determination of particle sizes. Environ Sci Technol 2009;43:7277–84.
Duggen S, Olgun N, Croot P, Hoffmann L, Dietze H, Delmelle P, et al. The role of airborne volcanic ash for the surface ocean biogeochemical iron-cycle: a review. Biogeosciences 2010;7:827–44.
Fan S, Moxim WJ, Levy H. Aeolian input of bioavailable iron to the ocean. Geophys Res Lett 2006;33:L07602.
Hoffmann LJ, Breitbarth E, Ardelan MV, Duggen S, Olgun N, Hassellöv M, et al. Influence of trace metal release from volcanic ash on growth of *Thalassiosira pseudonana* and *Emiliania huxleyi*. Mar Chem 2012;132–133:28–33.
Kadar E, Costa V, Santos RS, Powell JJ. Enrichment in trace metals Al Mn Co Cu Mo Cd Fe Zn Pb and Hg. of macro-invertebrate habitats at hydrothermal vents along the Mid Atlantic Ridge. Hydrobiology 2005;548:191–205.
Kadar E, Fisher A, Stolpe B, Harrison RM, Parello F, Lead J. Metallic nanoparticle enrichment at low temperature, shallow CO_2 seeps in Southern Italy. Mar Chem 2012;140–141:24–32.
Kadar E, Al-Subiai SN, Dyson O, Handy RD. Are reproduction impairments of free spawning marine invertebrates exposed to zero-valent nano iron associated with dissolution of nanoparticles? Nanotoxicology 2013;7:135–43.

Langmann B, Zaksek K, Hort M, Duggen S. Volcanic ash fertiliser for the surface ocean. Atmos Chem Phys 2010;10:3891–9.
Luo C, Mahowald NM, Meskhidze N, Chen Y, Siefert RL, Baker A, et al. Estimation of iron solubility from observations and a global aerosol model. J Geophys Res 2005;110. D23307.
Meskhidze N, Chameides WL, Nenes A. Dust and pollution: a recipe for enhanced ocean fertilization? J Geophys Res 2005;110:1–23.
Miller WL, King DW, Lin J, Kester DR. Photochemical redox cycling of iron in coastal sea water. Mar Chem 1995;50:63–77.
Okin GS, Bullard JE, Reynolds RL, Ballantine JAC, Schepanski K, Todd MC, et al. Dust: small-scale processes with global consequences. EOS Trans Am Geophys Union 2011;92:241–2.
Olgun N, Duggen S, Croot PL, Delmelle P, Dietze H, Schacht U, et al. Surface ocean iron fertilization: the role of subduction zone and hotspot volcanic ash and fluxes into the Pacific Ocean. Global Biogeochem Cycles 2011;25:GB4001.
Raiswell R. Iceberg-hosted nanoparticulate Fe in the Southern Ocean: mineralogy, origin, dissolution kinetics and source of bioavailable Fe. Deep Sea Res Part II 2011;58:1364–75.
Raiswell R, Benning LG, Davidson L, Tranter M. Nanoparticulate bioavailable iron minerals in icebergs and glaciers. Mineral Mag 2008;72:345–8.
Rose AL, Waite TD. Effect of dissolved natural organic matter on the kinetics of ferrous iron oxygenation in seawater. Environ Sci Technol 2003;37:4877–86.
Sander SG, Koschinsky A. Metal flux from hydrothermal vents increased by organic complexation Nat. Geosciences 2011;4:145–50.
Shi Z, Krom M, Bonneville S, Baker A, Jickells T, Benning L. Formation of iron nanoparticles and increase in iron reactivity in the mineral dust during simulated cloud processing. Environ Sci Technol 2009;43:6592–6.
Shi Z, Krom M, Bonneville S, Baker A, Bristow C, Drake N, et al. Influence of chemical weathering and aging of iron oxides on the potential iron solubility of Moroccan dust during simulated atmospheric processing. Global Biogeochem Cycles 2011a;25:1–14.
Shi Z, Bonneville S, Krom M, Carslaw K, Jickells T, Baker A, et al. Dissolution kinetics of iron in the mineral dust at low pH during simulated atmospheric processing. Atmos Chem Phys 2011b;11:995–1007.
Smetacek V, Klaas C, Strass VH, Assmy P, Montresor M, Cisewski B, et al. Deep carbon export from a Southern Ocean iron-fertilized diatom bloom. Nature 2012;487:313–9.
Tagliabue A, Bopp L, Dutay JC, Bowie AR, Chever F, Jean-Baptiste P, et al. Hydrothermal contribution to the oceanic dissolved iron inventory. Nat Geosci 2010;3:252–6.
Utsunomiya S, Ewing RC. Application of high-angle annular dark field scanning transmission electron microscopy (HAADF-STEM), STEM-energy dispersive X-ray spectrometry (EDX), and energy-filtered (EF)-TEM to the characterization of nanoparticles in the environment. Environ Sci Technol 2003;37:786–91.
Viollier E, Inglett PW, Hunter K, Roychoudhury AN, Van Cappellen P. The ferrozine method revisited: Fe(II)/Fe(III) determination in natural waters. Appl Geochem 2000;15:785–90.
Wolff GA, Billett DSM, Bett BJ, Holtvoeth J, FitzGeorge-Balfour T, Fisher EH, et al. The effects of natural iron fertilisation on deep-sea ecology. PLoS One 2011;6:1–9.